J. Fluid Mech. (2016), *vol.* 799, *pp.* 334–351.
doi:10.1017/jfm.2016.352

Taylor–Couette turbulence at radius ratio $\eta = 0.5$: scaling, flow structures and plumes

Roeland C. A. van der Veen[1], Sander G. Huisman[1], Sebastian Merbold[2], Uwe Harlander[2], Christoph Egbers[2], Detlef Lohse[1,3] and Chao Sun[4,1,†]

[1]Physics of Fluids Group, MESA$^+$ Institute and J.M. Burgers Centre for Fluid Dynamics, University of Twente, P.O. Box 217, 7500AE Enschede, The Netherlands

[2]Department of Aerodynamics and Fluid Mechanics, Brandenburg University of Technology Cottbus-Senftenberg, Siemens-Halske-Ring 14, 03046 Cottbus, Germany

[3]Max Planck Institute for Dynamics and Self-Organization, Am Fassberg 17, 37077 Göttingen, Germany

[4]Center for Combustion Energy and Department of Thermal Engineering, Tsinghua University, Beijing 100084, PR China

(Received 23 August 2015; revised 10 May 2016; accepted 22 May 2016; first published online 23 June 2016)

Using high-resolution particle image velocimetry, we measure velocity profiles, the wind Reynolds number and characteristics of turbulent plumes in Taylor–Couette flow for a radius ratio of 0.5 and Taylor number of up to 6.2×10^9. The extracted angular velocity profiles follow a log law more closely than the azimuthal velocity profiles due to the strong curvature of this $\eta = 0.5$ set-up. The scaling of the wind Reynolds number with the Taylor number agrees with the theoretically predicted 3/7 scaling for the classical turbulent regime, which is much more pronounced than for the well-explored $\eta = 0.71$ case, for which the ultimate regime sets in at much lower Taylor number. By measuring at varying axial positions, roll structures are found for counter-rotation while no clear coherent structures are seen for pure inner cylinder rotation. In addition, turbulent plumes coming from the inner and outer cylinders are investigated. For pure inner cylinder rotation, the plumes in the radial velocity move away from the inner cylinder, while the plumes in the azimuthal velocity mainly move away from the outer cylinder. For counter-rotation, the mean radial flow in the roll structures strongly affects the direction and intensity of the turbulent plumes. Furthermore, it is experimentally confirmed that, in regions where plumes are emitted, boundary layer profiles with a logarithmic signature are created.

Key words: Taylor–Couette flow, turbulent boundary layers, turbulent flows

1. Introduction

The paradigmatic Taylor–Couette (TC) flow has long been a flow configuration of great interest to fluid dynamicists. It consists of flow between two coaxial cylinders that can rotate independently (see figure 1). This system has been used extensively as a model in fluid physics because it is a closed system, has a relatively simple

† Email address for correspondence: chaosun@tsinghua.edu.cn

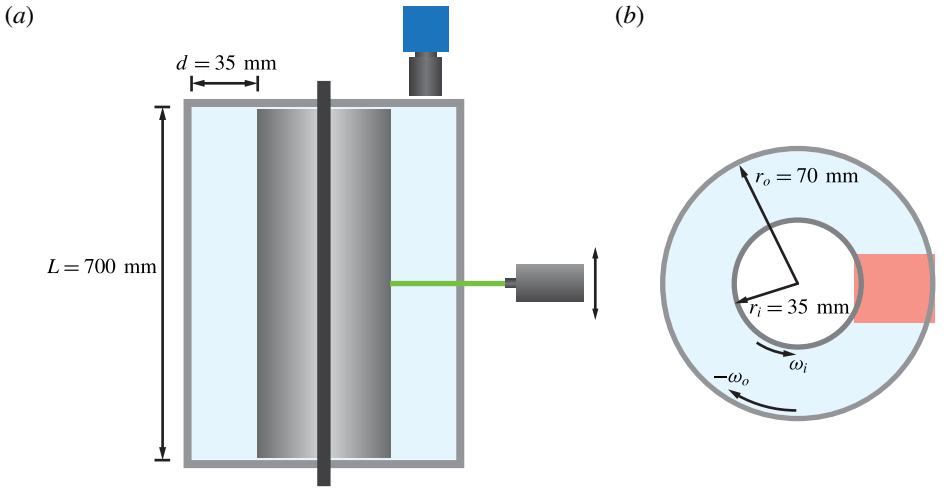

FIGURE 1. (Colour online) (*a*) Schematic of the vertical cross-section of the TC set-up, showing the horizontal laser sheet, which is imaged from above through the transparent top plate. The laser can be traversed vertically. (*b*) Horizontal cross-section of the set-up. The shaded red rectangle represents the typical field of view.

geometry and therefore has multiple symmetries. After early investigations (Couette 1890; Mallock 1896; Taylor 1923), Wendt (1933) started studying turbulence in this system. For a further historical overview, the reader is referred to Donnelly (1991). For a review on TC flow at the onset of instabilities and slightly above, see Fardin, Perge & Taberlet (2014). The state of the art of high-Reynolds-number TC turbulence is treated by Grossmann, Lohse & Sun (2016).

The two geometrical control parameters of TC flow are the ratio η of the inner and outer cylinder radii and the aspect ratio $\Gamma = L/d$, where d is the gap width and L is the height of the cylinders. In this work we use a small radius ratio of $\eta = 0.5$, corresponding to a relatively wide gap. The vast majority of existing work (see overview by Dubrulle *et al.* (2005) and review by Grossmann *et al.* (2016)) focuses on a radius ratio of 0.71 or higher. Lower-η experiments concern the Rayleigh-stable regime (Ji *et al.* 2006), mean flow and turbulence characteristics (van Hout & Katz 2011) and global torque measurements (Merbold, Brauckmann & Egbers 2013). In addition, numerical work has been done for $\eta = 0.5$ (Dong 2007; Chouippe *et al.* 2014; Ostilla-Mónico *et al.* 2014*c*). The radius ratio is a key control parameter (Eckhardt, Grossmann & Lohse 2007) in TC flow, and it has been found that a low-radius-ratio TC system behaves differently compared to higher-η set-ups in several aspects, which will be outlined below. The underlying reason for the different behaviour is the strong boundary layer asymmetry. Because the ratio of inner and outer boundary layer thicknesses scales as η^3 (Eckhardt *et al.* 2007), a strong asymmetry between the inner and outer boundary layers exists for small radius ratio.

As dimensionless control parameters of the system, we use the (negative) rotation ratio $a = -\omega_o/\omega_i$ and the Taylor number (Eckhardt *et al.* 2007):

$$Ta = \frac{(1+\eta)^4}{64\eta^2}\frac{(r_o - r_i)^2(r_i + r_o)^2(\omega_i - \omega_o)^2}{\nu^2}, \tag{1.1}$$

where $\omega_{i,o}$ are the angular velocities of the inner and outer cylinders, $r_{i,o}$ are the inner and outer cylinder radii, $\eta = r_i/r_o$ is the radius ratio, and ν is the kinematic viscosity. The driving of the system can also be described by the shear Reynolds number (Dubrulle *et al.* 2005):

$$Re_S = \frac{2r_i r_o (r_o - r_i)}{\nu (r_o + r_i)} |\omega_o - \omega_i|, \tag{1.2}$$

for which $Re_S \propto Ta^{1/2}$.

When increasing the driving strength (i.e. the Taylor number), TC flow first gradually undergoes a transition from a purely azimuthal, laminar state to a state where the bulk becomes turbulent while the boundary layers still remain laminar. The latter state is called the classical turbulent regime (Grossmann & Lohse 2000). By further increasing *Ta*, the ultimate turbulent regime (Kraichnan 1962; Grossmann & Lohse 2011; He *et al.* 2012) is reached, in which also the boundary layers are turbulent. The signature of these turbulent boundary layers are logarithmic velocity profiles, which have recently been found for a radius ratio of $\eta = 0.716$ (Huisman *et al.* 2013) and for $\eta = 0.909$ (Ostilla-Mónico *et al.* 2016). Grossmann, Lohse & Sun (2014) have derived theoretical velocity profiles, and found that the angular velocity profile follows a log law more closely than the azimuthal velocity profile, an effect that is more pronounced with the stronger asymmetry for smaller η. In § 3.1 we set out to investigate the correspondence of experimentally measured angular and azimuthal velocity profiles to a log law for $\eta = 0.5$ and Taylor numbers up to 6.2×10^9 at the onset of the ultimate turbulent regime. Furthermore, the velocity profiles are compared to existing experimental and numerical work.

In addition to affecting the velocity profiles, the radius ratio strongly influences the transitional Taylor number for the ultimate regime (Ravelet, Delfos & Westerweel 2010; Merbold *et al.* 2013; Ostilla-Mónico *et al.* 2014*a*,*c*). For $\eta = 0.5$ the ultimate regime does not start before $Ta = 10^{10}$ (Merbold *et al.* 2013; Ostilla-Mónico *et al.* 2014*c*), whereas the transition for a higher radius ratio of $\eta = 0.71$ already occurs at $Ta = 5 \times 10^8$ (van Gils *et al.* 2012; Ostilla-Mónico *et al.* 2014*c*). Very different scaling of the angular momentum transfer and the 'wind' in the gap with the driving parameter *Ta* exist for the classical and ultimate regimes (Grossmann & Lohse 2000, 2011). The degree of turbulence of the wind in the gap of the cylinders, which measures the strength of the secondary flows u_r and u_z, can be characterised by the wind Reynolds number. We use the standard deviation of the radial velocity $\sigma(u_r)$ to quantify the wind Reynolds number,

$$Re_w = \sigma(u_r) d/\nu, \tag{1.3}$$

with the gap width $d = r_o - r_i$. The late onset of the ultimate regime for $\eta = 0.5$ gives us the opportunity to analyse the scaling of the wind Reynolds number with Taylor numbers in the classical TC regime, up to the onset of the ultimate regime, and to compare it with theoretical predictions (§ 3.2). Furthermore, a similar analysis is performed on the standard deviation of the azimuthal velocity, leading to a scaling of the turbulence intensity, which is compared to that in Rayleigh–Bénard convection.

Another area where the influence of the radius ratio is apparent is the angular momentum transport through the gap. This transport is a key response parameter of the system and is directly connected to the torque required to maintain constant cylinder velocities (Eckhardt *et al.* 2007). The radius ratio strongly influences the

rotation ratio for which optimal momentum transport occurs (van Gils *et al.* 2012; Brauckmann & Eckhardt 2013; Merbold *et al.* 2013; Ostilla-Mónico *et al.* 2014*a*; Brauckmann, Salewski & Eckhardt 2016). For example, the optimal momentum transport occurs at $a_{opt} \approx 0.33$ for $\eta = 0.714$ (van Gils *et al.* 2012) whereas it is $a_{opt} \approx 0.20$ for $\eta = 0.5$ (Merbold *et al.* 2013).

Roll structures play an important role in the momentum transport in the TC system (Fenstermacher, Swinney & Gollub 1979; Andereck, Liu & Swinney 1986; Lewis & Swinney 1999; Huisman *et al.* 2014; Ostilla-Mónico *et al.* 2014*b*). With increasing Taylor number, the system undergoes transitions from a purely laminar state to having steady coherent Taylor vortices, to having modulated wavy Taylor vortices, which eventually evolve into chaotic turbulent Taylor vortices (Lewis & Swinney 1999). But even in the ultimate regime, for some $a > 0$, it was found that remnants of these rolls are present in time-averaged quantities (Tokgoz *et al.* 2011; Huisman *et al.* 2014; Ostilla-Mónico *et al.* 2014*b*), whereas for $a = 0$ (pure inner cylinder rotation) these rolls vanish for large Taylor number (Lathrop, Fineberg & Swinney 1992). In § 3.3 we will characterise the roll structures for $\eta = 0.5$ at both pure inner cylinder rotation $a = 0$ and slight counter-rotation $a = 0.2$, at which optimal transport occurs.

It was recently proposed that the logarithmic velocity profiles in ultimate TC flow are triggered by turbulent plume ejection (Ahlers, Bodenschatz & He 2014; Ostilla-Mónico *et al.* 2014*b*; van der Poel *et al.* 2015), which in turn is regulated by the relative strength of the axial and radial mean flows. Using time-resolved azimuthal and radial velocity field measurements at several heights in the set-up, we will investigate the connection between the roll structures that generate strong radial and axial flows, and the turbulent plumes that emanate from either the inner or outer cylinder (§ 3.4). Furthermore, in § 3.5 we will quantify how these plumes affect the logarithmic nature of the velocity profiles.

2. Set-up and explored parameter space

2.1. *Set-up*

The experiments were carried out in the Cottbus Taylor–Couette Facility (Merbold, Fischer & Egbers 2011; Merbold *et al.* 2013). The inner and outer cylinder radii are $r_i = 35.0 \pm 0.2$ mm and $r_o = 70.0 \pm 0.2$ mm, respectively, and the height of the set-up is $L = 700$ mm. This gives a radius ratio of $\eta = 0.5$ and an aspect ratio of $\Gamma = 20$. This aspect ratio is sufficiently large so that we do not expect the endwalls to significantly affect the velocity in the bulk (van Gils *et al.* 2012; Paoletti *et al.* 2012). The cylindricities of the cylinders that were used are 0.4 mm and 0.3 mm for the inner and outer cylinders, respectively. The maximum rotation rates are 5 Hz for both the inner and outer cylinders.

The end plates rotate with the outer cylinder. The outer cylinder and the top plate are transparent, making the set-up ideally suited to be used in combination with particle image velocimetry (PIV). A high-resolution PIV camera (LaVision Imager sCMOS) with a resolution of 2560×2160 pixels and a frame rate of 50 Hz is installed above the top end plate, pointing downwards. Water is used as the working fluid (20 °C, $\nu = 1.0 \times 10^{-6}$ m^2 s^{-1}). The water contains fluorescent particles (Dantec Dynamics, PMMA-RhB, 1–20 μm) with a maximum Stokes number of $St = \tau_p/\tau_\eta \approx 10^{-4} \ll 1$, which means that they faithfully follow the flow and can be considered as tracer particles. The flow is illuminated by a horizontal light sheet from a high-powered pulsed Nd:YLF dual-cavity laser (Litron LDY303HE). Because of the high-resolution PIV camera, very high-resolution measurements of the flow fields can

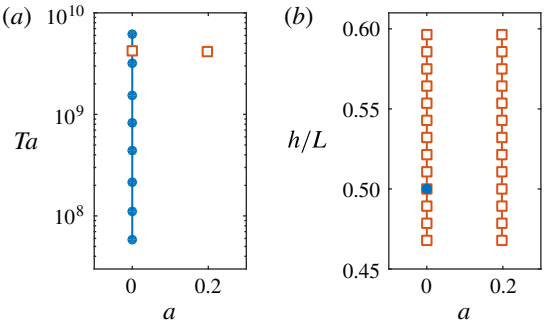

FIGURE 2. (Colour online) The explored parameter space. The Taylor number (Ta) is varied for inner cylinder rotation ($a = 0$), and axial scans have been performed for (negative) rotation ratios $a = 0$ and $a = 0.2$.

be achieved. The imaging of the full width of the gap combined with a vector grid of 16×16 pixels with 50 % overlap results in a velocity vector spacing of 0.13 mm. The PIV system is operated in dual frame mode, allowing for an inter-frame time Δt smaller than the inverse frame rate. The PIV image pairs are processed using LaVision DaVis software, after which the flow fields are transformed to the radial velocity $u_r(\theta, r, z, t)$ and the azimuthal velocity $u_\theta(\theta, r, z, t)$.

2.2. *Explored parameter space*

The parameter space that was explored for this work is shown in figure 2. The first set of measurements that is treated here consists of varying the Taylor number between $Ta = 5.8 \times 10^7$ and $Ta = 6.2 \times 10^9$ (corresponding to a shear Reynolds number of $Re_S = 6.0 \times 10^3$–6.2×10^4) for inner cylinder rotation only ($a = 0$) at mid-height ($h = 0.5L$). These measurements were performed as a single continuous experiment; the cylinder velocity was increased slowly between experiments, and before each measurement approximately 10 min were taken to give the flow ample time to stabilise. Each measurement in this set consists of 10 000 PIV image pairs, which were recorded at 25 frames per second (f.p.s.). This corresponds to 235 and 2418 cylinder revolutions for $Ta = 5.8 \times 10^7$ and $Ta = 6.2 \times 10^9$, respectively.

In addition to investigating the Taylor-number dependence, the height of the laser sheet was varied to characterise the axial dependence of the flow field. At 13 different heights with 7.5 mm spacing, 5000 image pairs of the velocity field were recorded. This was done at $Ta = 4.2 \times 10^9$ for both pure inner cylinder rotation and optimal (Merbold *et al.* 2013) counter-rotation $a = 0.2$.

3. Results

3.1. *Azimuthal and angular velocity profiles*

In this part the properties of flow profiles for varying Taylor number will be investigated. An example of an instantaneous flow field is shown in figure 3(*a*), while the averaged field is shown in figure 3(*c*). In figure 3(*b*) the normalised radial velocity $\tilde{u}_r = u_r/u_\theta(r_i)$ versus the dimensionless gap position $\tilde{r} = (r - r_i)/(r_o - r_i)$ is shown, from which it is apparent that, at this specific axial position (mid-height), a significant mean radial flow still exists for the lower Taylor numbers up to approximately 10^9.

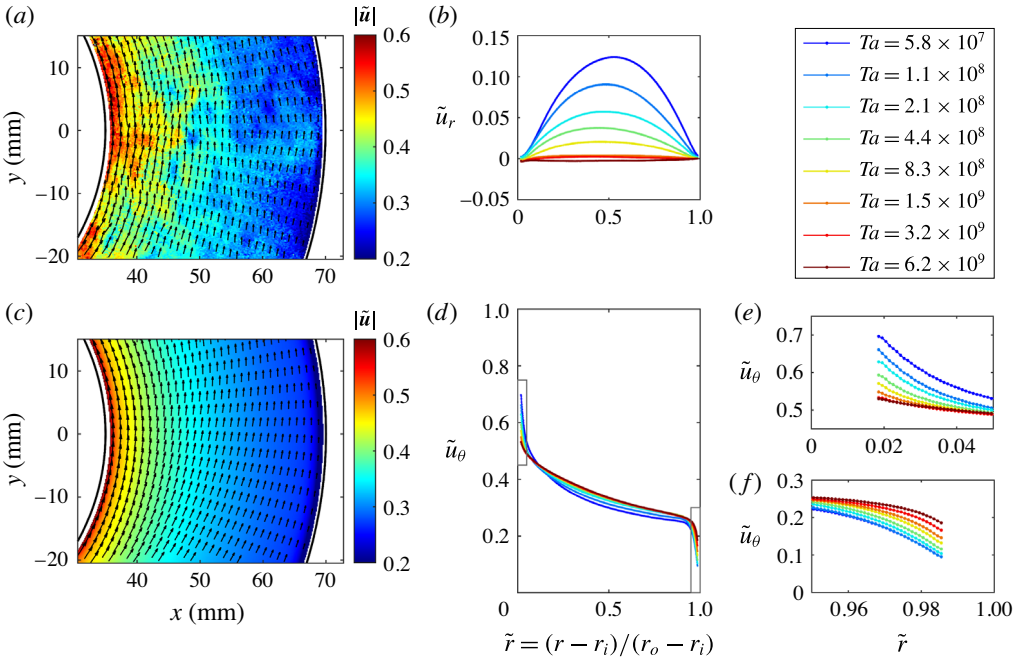

FIGURE 3. (Colour online) Overview of the flow profiles for varying Taylor number with pure inner cylinder rotation $a = 0$ at mid-height $h/L = 0.5$. (*a*) Snapshot of the flow field for $Ta = 6.2 \times 10^9$. The colours and lengths of the arrows indicate the norm of the velocity $|\tilde{\boldsymbol{u}}|$. (*c*) Averaged flow field over 10 000 PIV image pairs at $Ta = 6.2 \times 10^9$. (*b*) Radial velocity profiles across the gap of the TC apparatus, normalised by the inner cylinder velocity. For lower Taylor numbers, there is still a strong radial flow, which can be attributed to the presence of Taylor vortices. (*d*) Azimuthal velocity profiles normalised by the inner cylinder velocity. For increasing Taylor number, the profiles become flatter and the boundary layers steeper. (*e*,*f*) Magnification of the azimuthal velocity profiles in (*d*) close to the cylinders.

These are Taylor vortices, which at $a = 0$ disappear for higher Taylor numbers (Lathrop *et al.* 1992). With increasing Taylor number, the azimuthal velocity profile in the bulk becomes flatter (figure 3*d–f*), but it is still apparent that the strong curvature of a radius ratio of $\eta = 0.5$ creates a significant asymmetry between the inner and outer boundary layers.

In figure 4, profiles up to the middle of the gap are shown, normalised to the wall-normal distance y^+ from both the inner and outer cylinders, and to the azimuthal velocity u^+ (figure 4*a*,*b*) and angular velocity ω^+ (figure 4*c*,*d*). The wall-normal distance, azimuthal velocity and angular velocity for the inner cylinder are defined as

$$y^+ = \frac{r - r_i}{\delta_{v,i}}, \tag{3.1}$$

$$u^+ = \frac{u_\theta(r_i) - u_\theta(r)}{u_{\tau,i}}, \tag{3.2}$$

$$\omega^+ = \frac{\omega(r_i) - \omega(r)}{u_{\tau,i}/r_i}. \tag{3.3}$$

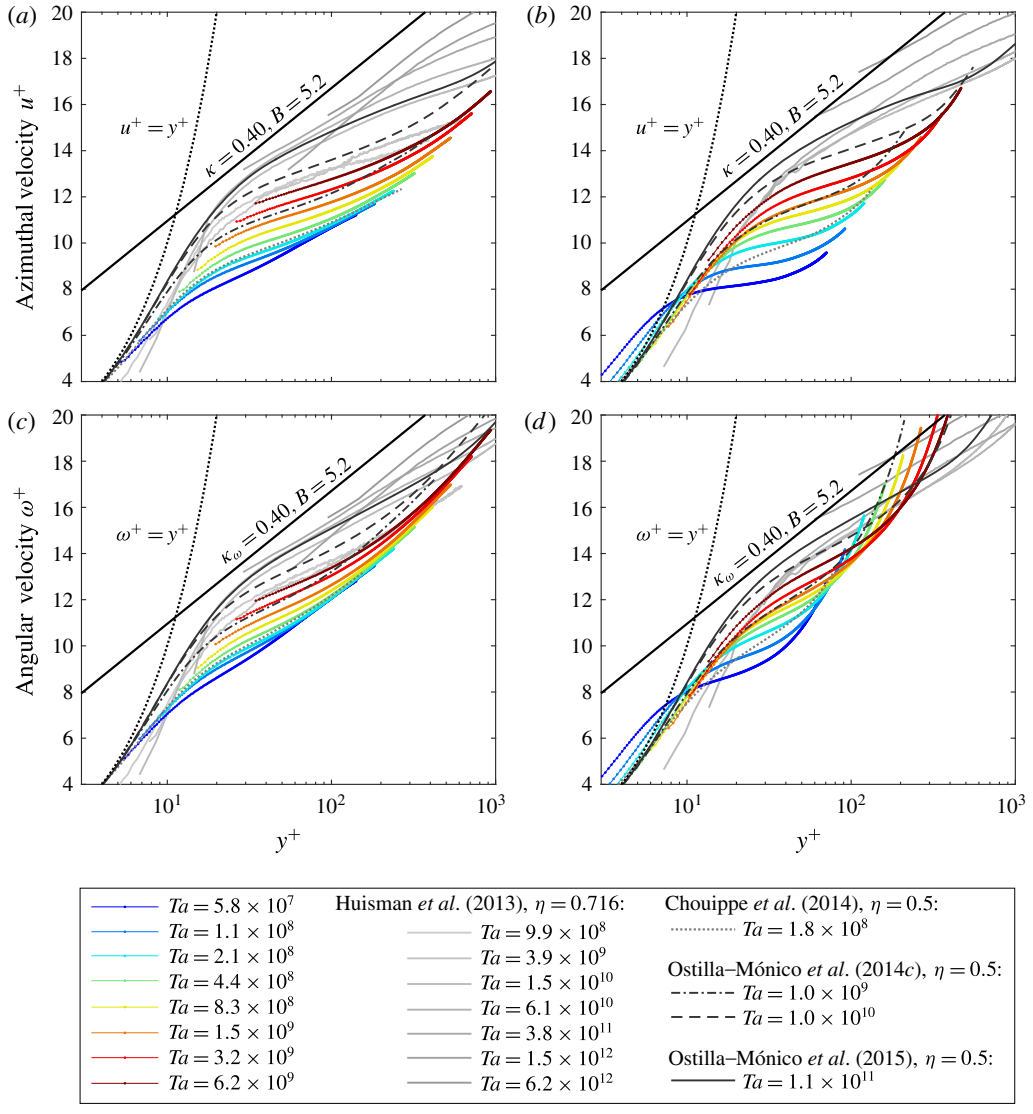

FIGURE 4. (Colour online) Velocity profiles for inner cylinder rotation $a = 0$ and varying Taylor number. See main text for the definitions of u^+, ω^+ and y^+. (*a*) Azimuthal velocity profiles near the inner cylinder ($\tilde{r} \in [0, 1/2]$). (*b*) Azimuthal velocity profiles near the outer cylinder ($\tilde{r} \in [1/2, 1]$). (*c*) Angular velocity profiles near the inner cylinder ($\tilde{r} \in [0, 1/2]$). (*d*) Angular velocity profiles near the outer cylinder ($\tilde{r} \in [1/2, 1]$). All panels include the logarithmic law of the wall from Prandtl and von Kármán, $u^+ = 1/\kappa \ln y^+ + B$, with the typical values of $\kappa = 0.40$ and $B = 5.2$ (see Marusic *et al.* (2013) and references therein), the viscous sublayer $u^+ = y^+$, direct numerical simulation data from Chouippe *et al.* (2014), Ostilla-Mónico *et al.* (2014*c*) and Ostilla-Mónico *et al.* (2016) at $\eta = 0.5$, and measurement data from Huisman *et al.* (2013) at $\eta = 0.716$.

The same parameters for the outer cylinder are defined as

$$y^+ = \frac{r_o - r}{\delta_{\nu,o}}, \tag{3.4}$$

$$u^+ = \frac{u_\theta(r) - u_\theta(r_o)}{u_{\tau,o}}, \tag{3.5}$$

$$\omega^+ = \frac{\omega(r) - \omega(r_o)}{u_{\tau,o}/r_o}, \tag{3.6}$$

with the viscous length scale $\delta_{v,i} = \nu/u_{\tau,i}$ and the friction velocity $u_{\tau,i} = \sqrt{\tau_{w,i}/\rho}$, containing the wall shear stress $\tau_{w,i} = T/2\pi r_i^2 L$, with the torque T, where the subscript i may be replaced by o. As a consequence, $\delta_{v,i}/\delta_{v,o} = \eta$, $u_{\tau,i}/u_{\tau,o} = 1/\eta$ and $\tau_{w,i}/\tau_{w,o} = 1/\eta^2$. The torque values are from Merbold *et al.* (2013), where a (non-transparent) TC set-up with identical dimensions and boundary conditions was used. The local torque can be different from the average torque, following the large-scale roll structures. This causes the imperfect matching with the viscous sublayer $u^+ = y^+$ and $\omega^+ = y^+$, especially visible in figure 4(*b*,*d*).

As the driving is increased, the profiles slowly approach the Prandtl–von Kármán log law, although at these Taylor numbers the log layer is not yet fully developed. For comparison, profiles at higher Taylor numbers and aspect ratio of $\eta = 0.716$ from Huisman *et al.* (2013) are also plotted. The data show good agreement with direct numerical simulations (DNS) at the same radius ratio $\eta = 0.5$ from Chouippe *et al.* (2014) at $Ta = 1.8 \times 10^8$, Ostilla-Mónico *et al.* (2014*c*) at $Ta = 1.0 \times 10^9$ and $Ta = 1.0 \times 10^{10}$, and Ostilla-Mónico *et al.* (2016) at $Ta = 1.1 \times 10^{11}$.

When comparing the azimuthal velocity u^+ to the angular velocity ω^+, i.e. figure 4(*a*) to 4(*c*) and figure 4(*b*) to 4(*d*), it can be seen that the angular velocity profiles curve upwards more compared to the azimuthal ones. This is consistent with the theoretical argument of Grossmann *et al.* (2014) that the angular velocity profile ω^+ is closer to a log law than the azimuthal velocity profile u^+. The effect is much more pronounced for the smaller $\eta = 0.5$ here as compared to the $\eta = 0.716$ from Huisman *et al.* (2013). Note that, for example, the lower-Taylor-number u^+ profiles at $\eta = 0.716$ are above the profiles measured here, but that they cross when represented as ω^+. This clearly shows the influence of the large curvature for small-radius-ratio TC set-ups.

3.2. *Wind Reynolds number and turbulence intensity*

In the analogy between TC and Rayleigh–Bénard flow, the unifying theory of Grossmann & Lohse (2000) predicts that the wind Reynolds number in the classical turbulent regime scales as

$$Re_w \propto Ta^{3/7}. \tag{3.7}$$

In contrast, in the ultimate turbulent regime, the scaling was predicted to be $Re_w \propto Ta^{1/2}$ (Grossmann & Lohse 2011), which was confirmed experimentally by Huisman *et al.* (2012) for TC flow with $\eta = 0.716$ for Ta up to 6.2×10^{12}.

The highest Taylor number we achieve in the present measurements is $Ta = 6.2 \times 10^9$, which for $\eta = 0.5$ with the higher transitional Taylor number of $Ta = 10^{10}$ (Merbold *et al.* 2013; Ostilla-Mónico *et al.* 2014*c*) implies that we are in the classical turbulent regime. Therefore we expect the theoretically predicted 3/7 scaling to hold. This classical scaling was measured in Rayleigh–Bénard convection (He *et al.* 2012), but to our knowledge has not yet been confirmed for TC flow.

The wind Reynolds number Re_w is extracted from the velocity field $u_r(\theta, r, z, t)$ by calculating the standard deviation $\sigma(u_r(r, \theta, t))$ over time and the azimuthal direction, which is then averaged over a certain range in the gap (see figure 5). When looking

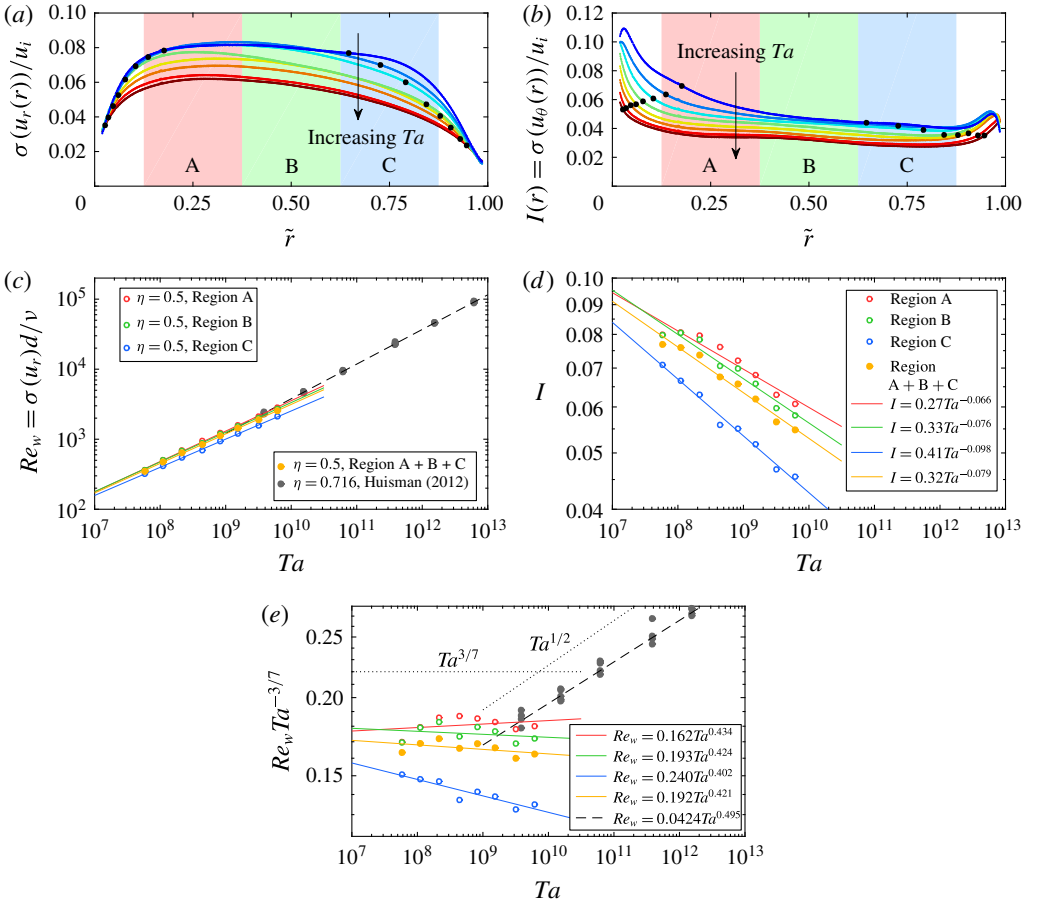

FIGURE 5. (Colour online) The scaling of the wind Reynolds number Re_w and turbulence intensity I with Taylor number for inner cylinder rotation $a = 0$. (*a*,*b*) The standard deviation of the radial velocity (*a*) and azimuthal velocity (*b*) over 10 000 frames (400 s) and the azimuthal direction, normalised by the inner cylinder velocity, as a function of the normalised radial position. This corresponds to the turbulence intensity I in the case of the azimuthal velocity. See the legend in figures 3 or 4 for the values of the Taylor numbers. The three areas A ($\tilde{r} \in [1/8, 3/8]$), B ($\tilde{r} \in [3/8, 5/8]$) and C ($\tilde{r} \in [5/8, 7/8]$) indicate regions over which σ is averaged for (*c–e*). The black dots represent the position of the start of the outer layers at $y^+ = 50$. (*c*) Plot showing Re_w versus Ta averaged over $\tilde{r}$ values corresponding to regions A, B, C and all three combined ($\tilde{r} \in [1/8, 7/8]$). In addition, data from Huisman *et al.* (2012) at $\eta = 0.716$ with their fit are shown, which are fully in the ultimate turbulent regime. These data use the equivalent to area B for averaging. (*d*) Turbulence intensity I versus Ta averaged over the same regions as before. The fits are $I = 0.27Ta^{-0.066}$ for area A, $I = 0.33Ta^{-0.076}$ for area B, $I = 0.41Ta^{-0.098}$ for area C and $I = 0.32Ta^{-0.079}$ for the three areas combined. (*e*) Data in (*c*) compensated by $Ta^{3/7}$. The fits are $Re_w = 0.162Ta^{0.434}$ for area A, $Re_w = 0.193Ta^{0.424}$ for area B, $Re_w = 0.240Ta^{0.402}$ for area C and $Re_w = 0.192Ta^{0.421}$ for the three areas combined. The standard errors of the fitted exponents are 0.007, 0.007, 0.005 and 0.005, respectively.

at the shape of the $\tilde{r}$ dependence of $\sigma(u_r)$ in figure 5(*a*), it is apparent that an asymmetry is present. The fluctuations exhibit a maximum around a quarter of the gap width away from the inner cylinder. It is likely that the strong curvature of the

$\eta = 0.5$ set-up causes this asymmetry. Calculating the wind Reynolds number thus comes with an arbitrariness in the area to choose for averaging the profile of $\sigma(r)$, although excluding the boundary layers is reasonable because the interest lies in the convective bulk transport, as opposed to the diffusive transport in the boundary layers. The dependence of $Re_w(Ta)$ is shown in figure 5(*c*) for different regions of averaging. Region B lies within the outer layer of both the inner and outer cylinders for all Taylor numbers.

From figure 5(*e*) it can be seen that a clear power-law scaling is present, with an exponent that ranges from 0.402 to 0.434, depending on the region of averaging. The scaling in regions A, B and A + B + C is consistent with the theoretically predicted classical regime scaling of $3/7 \approx 0.429$ (Grossmann & Lohse 2000) within the experimental uncertainties.

A similar analysis is performed on the azimuthal velocity instead of the radial velocity, as shown in figure 5(*b*,*d*). Again, the difference of the shearing velocity $(u_i - u_o)$, which in the case of $a = 0$ simplifies to u_i, is used to normalise the standard deviation. This results in a turbulence intensity $I = \sigma(u_\theta)/u_i$, analogous to the turbulence intensity defined in Rayleigh–Bénard convection. The difference in rotation velocities of TC flow is analogous to the temperature difference in Rayleigh–Bénard convection (Grossmann & Lohse 2000). We find that the turbulence intensity has maxima in both the boundary layers, similar to the findings of Huisman *et al.* (2013), and a relatively flat region in the bulk. The turbulence intensity $I(r)$ is averaged over the same regions as in figure 5(*a*) and shows negative scaling: $I \propto Ta^{\gamma}$ with $-0.1 < \gamma < -0.07$, depending on the region of averaging. This result is in rough agreement with the findings in Rayleigh–Bénard flow (Shang, Tong & Xia 2008; Lakkaraju *et al.* 2012), where the authors found a scaling exponent of $-0.2 < \gamma_{RB} < -0.1$ in the classical regime, depending on the Rayleigh number and the location of the temperature measurements. It is expected that $\gamma \to 0$ for $Re \to \infty$, possibly explaining the higher exponent measured here because of a more turbulent system. Additionally, TC flow, with its curved boundaries, might have a fundamentally different scaling exponent.

3.3. *Roll structures*

The phenomena of roll structures, turbulent plumes and logarithmic velocity profiles in TC flow are intimately connected (Ostilla-Mónico *et al.* 2014*b*,*c*). We will first show an example of roll structures that are observed in TC flow. Flow profiles at several heights for both $a = 0$ and $a = 0.2$ are measured, allowing us to visualise roll structures as shown in figure 6. At this reasonably high Taylor number of $Ta = 4.2 \times 10^9$, no clear roll structures exist for inner cylinder rotation only. The radial velocity shows some very faint indications of rolls, with a maximum value of $\tilde{u}_r = 0.01$ in the centre of the gap. In contrast, in the case of counter-rotation ($a = 0.2$), very strong roll structures can be seen. The fact that there are strong rolls at optimal counter-rotation and no clear structures at inner cylinder rotation only is corroborated by recent work for higher radius ratio (Tokgoz *et al.* 2011; Huisman *et al.* 2014; Ostilla-Mónico *et al.* 2014*b*).

In the radial flow between two rolls at approximately $h/L = 0.50$ to $h/L = 0.52$, there is very strong outwards radial flow (see figure 6*c*). Specifically, the height $0.52L$ corresponds to the bottom of a roll, while $0.50L$ corresponds to the top of the roll below. Exactly in between the rolls at $0.51L$, the radial flow surprisingly exhibits a local minimum. One might *a priori* expect symmetry around mid-height ($0.50L$) instead of at $0.51L$ as observed. However, symmetry breaking of large-scale turbulent

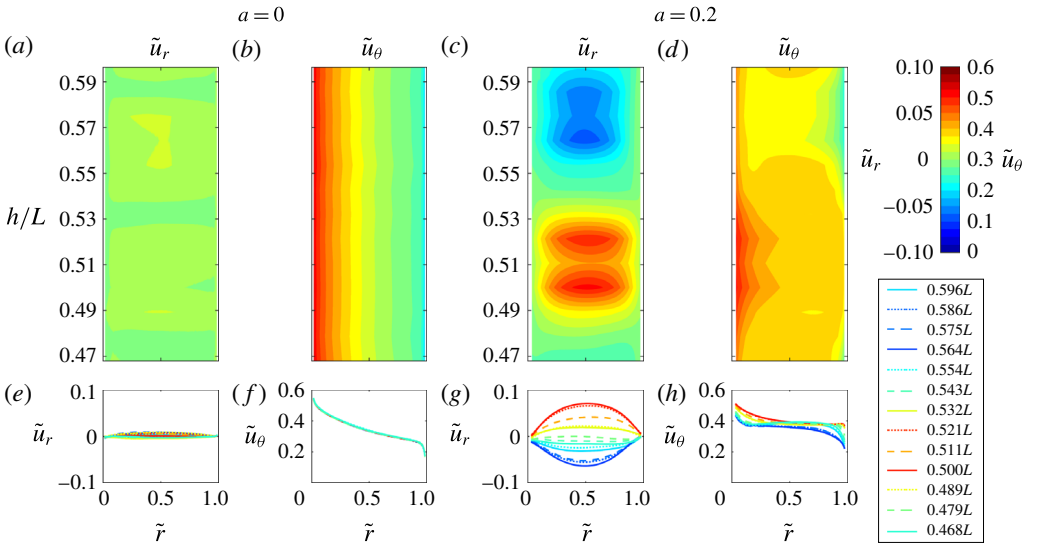

FIGURE 6. (Colour online) Dependence of flow profiles on axial position for rotation ratios $a=0$ (a,b,e,f) and $a=0.2$ (c,d,g,h) for $Ta=4.2\times10^9$. The normalised radial velocity is $\tilde{u}_r=u_r(r)/(u_i-u_o)$ and the azimuthal velocity is $\tilde{u}_\theta=(u_\theta(r)-u_o)/(u_i-u_o)$. The data are represented in a colour map (a–d) and as profiles in (e–h).

flow structures in symmetrical set-ups has been observed before, not only in TC flow (Huisman *et al.* 2014; van der Veen *et al.* 2016), but also in von Kármán flow (López-Caballero & Burguete 2013). In figure 6(d,h) it can be seen that, in the case of positive (outward) radial flow, the inner cylinder velocity is advected outwards, shifting the profiles upwards at the inner half of the gap. For negative (inward) radial flow, the profiles shift downwards in the outer half of the gap. In summary, the roll structures are represented by a large secondary flow of u_r, which advects velocity from the cylinders and changes the azimuthal velocity profiles. In the following two subsections we will elaborate on the characteristics of turbulent plumes and their effect on the velocity profiles.

3.4. *Turbulent plumes*

In turbulent TC flow, structures detach from the boundary layers, called herring-bone streaks (Dong 2007) or velocity plumes (Ostilla-Mónico *et al.* 2014*b*), in correspondence to the thermal plumes in the analogous turbulent Rayleigh–Bénard convection. These plumes in TC flow are large-scale spatial and temporal fluctuations in the velocity fields that detach from either the inner or outer cylinder and advect velocity from the respective cylinder. Because of the sufficiently high frame rate of 25 f.p.s. and large amount of data recorded in our experiments, these plumes can be resolved in time, and the typical velocity can be extracted. We are interested in understanding how these plumes are affected by roll structures and whether some scaling relation exists for the typical plume velocity as a function of the driving parameter Ta.

The time dependence of the profiles of the azimuthal and radial velocity can be represented by the spatio-temporal fields $u_r(r,\,t)$ and $u_\theta(r,\,t)$, with the value of the velocities represented by a colour map, as shown in figure 7(a), for example.

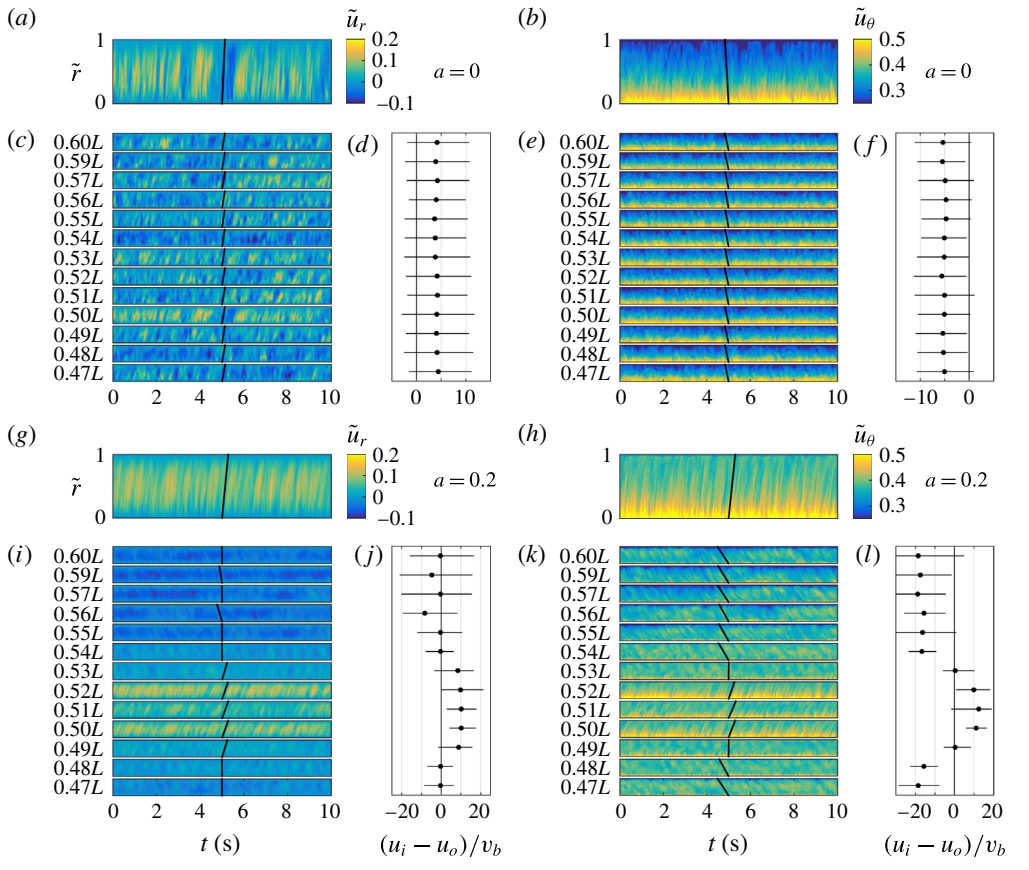

FIGURE 7. (Colour online) Overview of turbulent burst velocity depending on axial position, for both pure inner cylinder rotation $a = 0$ (*a–f*) and counter-rotation of $a = 0.2$ (*g–l*), at $Ta = 4.2 \times 10^9$. The radial velocity dependence is shown in (*a*,*c*,*d*,*g*,*i*,*j*) and the azimuthal velocity in (*b*,*e*,*f*,*h*,*k*,*l*). (*a*,*b*,*g*,*h*) Example of the radial and azimuthal velocity as a function of the normalised gap distance and time for the axial position of 0.50*L*. Only 10 s of the total 200 s per experiment are shown for clarity. Diagonal lines with a positive (negative) slope correspond to plumes coming from the inner (outer) cylinder. The extracted plume velocity (see text for method) is shown as a black line. (*c*,*e*,*i*,*k*) As above, for every height normalised by the total height of the cylinder *L*. (*d*,*f*,*j*,*l*) The inverse of the resulting normalised burst velocity. For $a = 0$ the inner cylinder velocity is 1.1 m s^{-1} and for $a = 0.2$ the inner and outer cylinder velocities are 0.91 m s^{-1} and -0.36 m s^{-1}, respectively. The error bars show the width of the test function at 0.95 times the peak value.

In this way, structures or fluctuations of the profiles that propagate inwards or outwards become visible as diagonal lines. It has to be stressed that these diagonals do not represent a non-zero mean radial flow, but only the fluctuations on these profiles that travel outwards or inwards. In order to assign a velocity to these plumes, we employ an analysis that is based on applying the following affine shearing transformation to the functions $u_r(r, t)$ and $u_\theta(r, t)$:

$$(r, t) \mapsto (r, t + d \cdot \tilde{r}/v_b), \tag{3.8}$$

with $\tilde{r} = (r - r_i)/d$, gap width d and plume velocity v_b. For a certain amount of shearing, the plumes that were represented by diagonal lines become vertical lines. To find this optimal value of shearing, we postulate that, when averaging the sheared function over $\tilde{r}$, the standard deviation of the resulting time signal has a maximum as a function of the shearing value. At this optimal shearing, the plumes are represented by narrow peaks in the time signal, creating a high standard deviation. Using a golden section search algorithm (Kiefer 1953), the optimal shearing value is found, which corresponds to the characteristic plume velocity v_b. Note that plumes can go both inwards and outwards and that this v_b corresponds to the 'strongest' plume direction, not necessarily to the mean plume velocity.

The dependence of the plume velocity on the axial position and the rotation ratio is shown in figure 7. Again, for inner cylinder rotation only ($a = 0$), no height dependence can be seen. The fluctuations on the radial velocity are moving outwards with a velocity $v_b/(u_i - u_o) = 0.25 \pm 0.02$ ($u_o = 0$, 2σ error). When the azimuthal velocity is considered, the picture looks different. Crossing diagonal lines can be seen, meaning that plumes emit from both the inner and outer cylinders. A maximum was found for inward plumes with an average velocity of $v_b/(u_i - u_o) = -0.20 \pm 0.02$. The velocity of these plumes is of the same order, but it remains to be explained why the main plume direction is different for the two velocity components.

For counter-rotation ($a = 0.2$), the bottom half of figure 7 clearly indicates that roll structures are present. There is a correspondence between the sign of the mean radial velocity and the direction of these turbulent plumes, coming from either the inner or outer cylinder – compare figure 6(*c*) with figure 7(*i*,*k*). For both velocity components, the direction of the plumes corresponds to the direction of the mean radial velocity. The mean radial velocity forces the plumes strongly in the inward or outward direction, also typically creating a higher plume velocity than for the $a = 0$ case. Whereas for the $a = 0$ case there was some ambiguity in the direction of the plumes for the azimuthal velocity, for $a = 0.2$ it exactly follows the roll structure. When looking at the radial velocity, the inward plumes are less pronounced than the outward ones, likely due to a tendency for the u_r plumes to flow outwards, as could be seen for the $a = 0$ case.

In addition to the dependence on the axial position and the rotation ratio, in figure 8 the dependence of the plume velocity on the driving parameter Ta is shown. With increasing driving strength, the velocity of the plumes also increases. When the plume velocity is normalised by $(u_i - u_o)$, it is however nearly constant over two decades of Ta.

3.5. *Logarithmic velocity profiles*

It has been proposed that the logarithmic temperature profiles in Rayleigh–Bénard convection and logarithmic velocity profiles in TC flow are triggered by plume ejection (Ahlers *et al.* 2014; Ostilla-Mónico *et al.* 2014*b*; van der Poel *et al.* 2015). These authors also support the notion that parts of the boundary layer can be turbulent, while others are not, and that the transition to the ultimate regime entails plume emission from the full extent of the boundary layer.

We will now further investigate the effect of the plumes on the logarithmic nature of the velocity profiles. As we have seen before, the roll structure that appears for counter-rotation of $a = 0.2$ provides strong mean radial flows, which cause plume emission away from either the inner or outer cylinder.

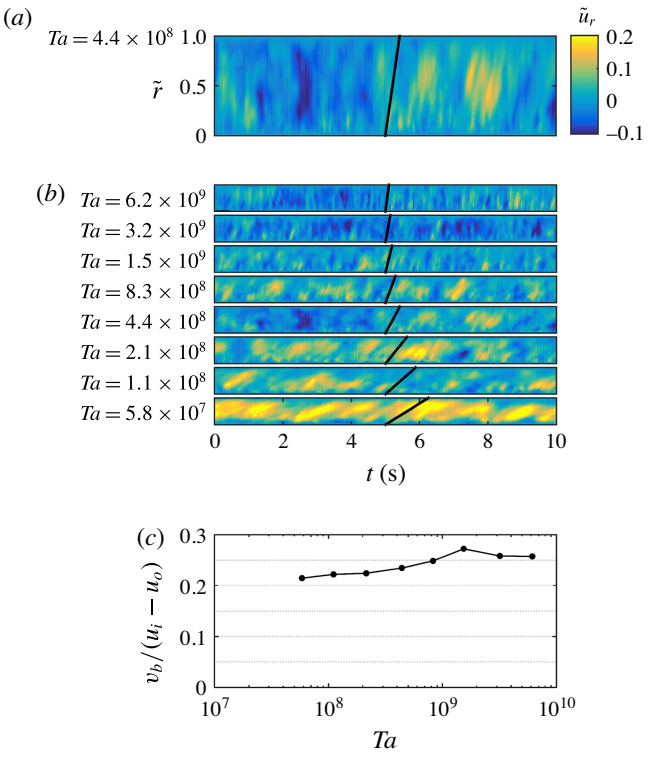

FIGURE 8. (Colour online) Turbulent plumes in the radial velocity for varying Ta and $a = 0$. (*a*,*b*) As in figure 7. (*c*) The plume velocity normalised by the inner cylinder velocity ($u_o = 0$). Errors are of the same order as in figure 7(*d*).

In figure 9(*a*) the angular velocity at the inner cylinder is shown. It can be seen that there is a significant variation in the shape of the profiles, and that profiles at the axial positions where a strong positive radial flow exists (top lines in figure 9*c*) follow the shape of a logarithmic law more closely. This effect is even stronger at the outer cylinder in figure 9(*b*), where profiles at an axial position with negative radial flow, so a flow away from the outer cylinder, correspond best to a log law.

To quantify this phenomenon, the velocity profiles are fitted with the modified (Grossmann *et al.* 2014) Prandtl–von Kármán law of the wall: $\omega^+ = 1/\kappa_\omega \ln y^+ + B$, with both κ_ω and B as fitting parameters. We quantify the deviation from a log profile by the standard error of the fitting parameter $\sigma(\kappa_\omega)$. A small value of $\sigma(\kappa_\omega)$ corresponds to a profile that closely follows a log law. In figure 9(*d*) it can be seen that, for a mean wall-normal velocity away from the cylinder (positive $\langle \tilde{\boldsymbol{u}} \cdot \boldsymbol{n} \rangle$), the value of κ_ω more closely approaches the known classical value of 0.40. Additionally, the error of the fit is much smaller for positive values of the outward wall-normal velocity as compared to negative values. This means that, for regions with strong radial flow away from a cylinder surface, the velocity profiles follow a log law more closely. In the previous section it was found that, at these regions, plumes are emitted from the cylinder surface. We therefore postulate that turbulent plumes are responsible for logarithmic boundary layers. This is in line with results from DNS (van der Poel *et al.* 2015; Ostilla-Mónico *et al.* 2014*b*).

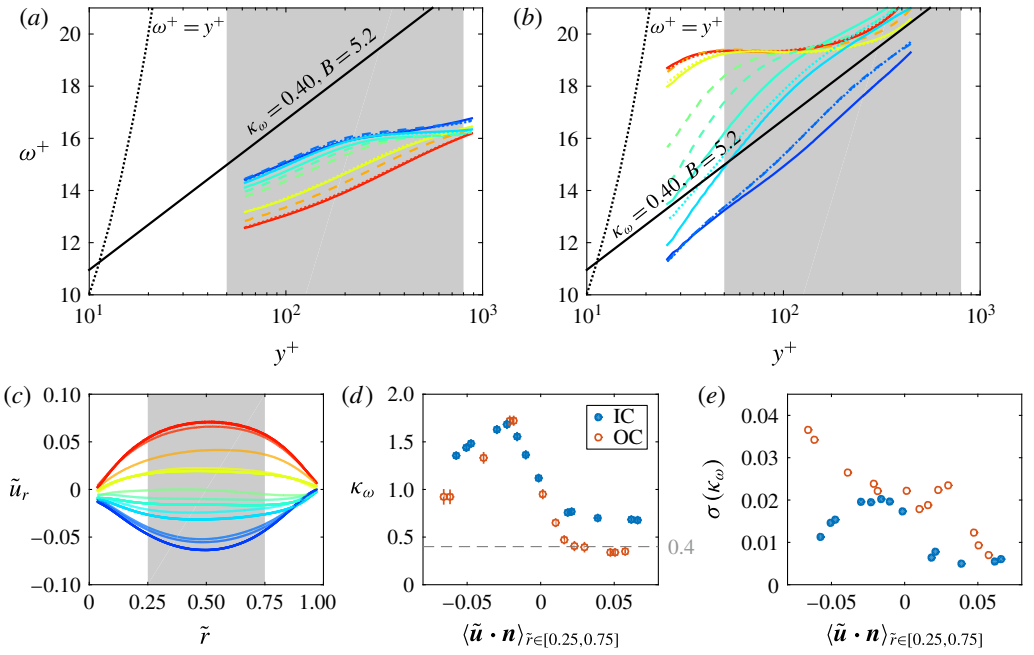

FIGURE 9. (Colour online) Angular velocity profile dependence on mean radial flow for counter-rotation $a = 0.2$ and $Ta = 4.2 \times 10^9$ at varying axial positions (data from figure 6*h*). (*a*) Angular velocity profiles near the inner cylinder ($\tilde{r} \in [0, 1/2]$). The angular velocity ω^+ and wall-normal distance y^+ are defined in the caption of figure 4, the colours and line styles of the profiles correspond to those in figure 6. The grey area is the fitting domain $y^+ \in [50, 800]$, chosen to encompass the start of the outer region up to mid-gap for both inner and outer cylinders. (*b*) Angular velocity profiles near the outer cylinder ($\tilde{r} \in [1/2, 1]$). (*c*) Normalised radial velocity $\tilde{u}_r$ as in figure 6(*g*). (*d*) The von Kármán constant κ_ω found by fitting $\omega^+ = 1/\kappa_\omega \ln y^+ + B$ for $y^+ \in [50, 800]$ near the inner (IC) and outer (OC) cylinder. The horizontal axis shows the normalised wall-normal velocity, equal to $\tilde{u}_r$ and $-\tilde{u}_r$ for the IC and OC, respectively, averaged over $\tilde{r} \in [1/4, 3/4]$. The error bars have a total length of four times the standard error of the fit. (*e*) The standard error of the fitting parameter κ_ω.

4. Conclusions

In this work, we measured velocity profiles, the wind Reynolds number and characteristics of turbulent plumes in TC flow for a radius ratio of 0.5 and Taylor number of up to 6.2×10^9. The flow profiles show Taylor vortices for a Taylor number smaller than $Ta \approx 10^9$. The normalised profiles approach the Prandtl–von Kármán log law, although at the highest $Ta = 6.2 \times 10^9$ the log layer is not yet fully developed. They are in good agreement with DNS data from other work (Chouippe *et al.* 2014; Ostilla-Mónico *et al.* 2014*c*; Ostilla-Mónico *et al.* 2016). Owing to the strong curvature of this $\eta = 0.5$ set-up, a large difference between the azimuthal velocity u^+ and the angular velocity ω^+ arises. The angular velocity ω^+ resembles a log law more closely, as suggested by Grossmann *et al.* (2014), based on their Navier–Stokes based theoretical considerations.

Because of the late onset of the ultimate regime for $\eta = 0.5$, the measurements with Ta up to 6.2×10^9 are in the classical turbulent regime. For the first time, the wind

Reynolds number has been measured in the classical regime of TC flow, and it indeed follows the theoretically predicted classical scaling of $Re_w \propto Ta^{3/7}$. The scaling of the turbulence intensity was found to be $I \propto Ta^{\gamma}$ with $-0.1 < \gamma < -0.07$, depending on the position in the gap.

Moreover, we focused on the interplay between rolls, turbulent plumes and logarithmic velocity profiles. At a strong driving of $Ta = 4.2 \times 10^9$, no significant coherent structures exist for pure inner cylinder rotation, but roll structures appear for counter-rotation at $a = -\omega_o/\omega_i = 0.2$. This behaviour has been observed previously for different values of η and Ta, and shows the important part that rolls play in momentum transfer between the two cylinders.

For inner cylinder rotation only, strong outward plumes are visible in the radial velocity. In the azimuthal velocity, the plumes mainly go inwards. The exact mechanism causing this difference is yet to be elucidated. For counter-rotation, the roll structures strongly influence the direction of the plumes. There is a direct correspondence between the direction of the mean radial flow and the direction of the plumes at a certain position. The plume velocity in the radial flow profiles increases with Taylor number, and has an approximately constant value of one-quarter of the inner cylinder velocity for pure inner cylinder rotation.

Lastly, by quantifying the correspondence of the angular velocity profiles to a log law for several axial positions, it was found that, in regions with strong radial flow away from a cylinder surface, plumes will emit from that cylinder, which in turn create logarithmic boundary layers.

This work confirms predictions about velocity profiles and the scaling of the wind Reynolds number and sheds new light on the characteristics and the role of plumes in TC flow for a radius ratio $\eta = 0.5$, and hopefully will spark further research into these intricate phenomena.

Acknowledgements

We thank the technicians of the Department of Aerodynamics and Fluid Mechanics at the BTU for their technical support. This work was financially supported by the European High-Performance Infrastructures in Turbulence (EuHIT), COST Action MP1305, a European Research Council (ERC) Advanced Grant, and the Simon Stevin Prize of the Technology Foundation STW of The Netherlands. C.E. and S.M. acknowledge the financial support of DFG (FOR 118, EG 100/15-2).

REFERENCES

AHLERS, G., BODENSCHATZ, E. & HE, X. 2014 Logarithmic temperature profiles of turbulent Rayleigh–Bénard convection in the classical and ultimate state for a Prandtl number of 0.8. *J. Fluid Mech.* **758**, 436–467.

ANDERECK, C. D., LIU, S. S. & SWINNEY, H. L. 1986 Flow regimes in a circular Couette system with independently rotating cylinders. *J. Fluid Mech.* **164**, 155–183.

BRAUCKMANN, H. J. & ECKHARDT, B. 2013 Intermittent boundary layers and torque maxima in Taylor–Couette flow. *Phys. Rev.* E **87**, 033004.

BRAUCKMANN, H. J., SALEWSKI, M. & ECKHARDT, B. 2016 Momentum transport in Taylor–Couette flow with vanishing curvature. *J. Fluid Mech.* **790**, 419–452.

CHOUIPPE, A., CLIMENT, E., LEGENDRE, D. & GABILLET, C. 2014 Numerical simulation of bubble dispersion in turbulent Taylor–Couette flow. *Phys. Fluids* **26** (4), 043304.

COUETTE, M. 1890 Études sur le frottement des liquides. *Ann. Chim. Phys.* **21**, 433.

DONG, S. 2007 Direct numerical simulation of turbulent Taylor–Couette flow. *J. Fluid Mech.* **587**, 373–393.

DONNELLY, R. J. 1991 Taylor–Couette flow: the early days. *Phys. Today* **44** (11), 32–39.

DUBRULLE, B., DAUCHOT, O., DAVIAUD, F., LONGGARETTI, P. Y., RICHARD, D. & ZAHN, J. P. 2005 Stability and turbulent transport in Taylor–Couette flow from analysis of experimental data. *Phys. Fluids* **17**, 095103.

ECKHARDT, B., GROSSMANN, S. & LOHSE, D. 2007 Torque scaling in turbulent Taylor–Couette flow between independently rotating cylinders. *J. Fluid Mech.* **581**, 221–250.

FARDIN, M. A., PERGE, C. & TABERLET, N. 2014 'The hydrogen atom of fluid dynamics' – Introduction to the Taylor–Couette flow for soft matter scientists. *Soft Matt.* **10**, 3523–3535.

FENSTERMACHER, P. R., SWINNEY, H. L. & GOLLUB, J. P. 1979 Dynamical instabilities and the transition to chaotic Taylor vortex flow. *J. Fluid Mech.* **94**, 103–128.

VAN GILS, D. P. M., HUISMAN, S. G., GROSSMANN, S., SUN, C. & LOHSE, D. 2012 Optimal Taylor–Couette turbulence. *J. Fluid Mech.* **706**, 118–149.

GROSSMANN, S. & LOHSE, D. 2000 Scaling in thermal convection: a unifying theory. *J. Fluid Mech.* **407**, 27–56.

GROSSMANN, S. & LOHSE, D. 2011 Multiple scaling in the ultimate regime of thermal convection. *Phys. Fluids* **23**, 045108.

GROSSMANN, S., LOHSE, D. & SUN, C. 2014 Velocity profiles in strongly turbulent Taylor–Couette flow. *Phys. Fluids* **26**, 025114.

GROSSMANN, S., LOHSE, D. & SUN, C. 2016 High Reynolds number Taylor–Couette turbulence. *Annu. Rev. Fluid Mech.* **48**, 53–80.

HE, X., FUNFSCHILLING, D., NOBACH, H., BODENSCHATZ, E. & AHLERS, G. 2012 Transition to the ultimate state of turbulent Rayleigh–Bénard convection. *Phys. Rev. Lett.* **108**, 024502.

VAN HOUT, R. & KATZ, J. 2011 Measurements of mean flow and turbulence characteristics in high-Reynolds number counter-rotating Taylor–Couette flow. *Phys. Fluids* **23** (10), 105102.

HUISMAN, S. G., VAN GILS, D. P. M., GROSSMANN, S., SUN, C. & LOHSE, D. 2012 Ultimate turbulent Taylor–Couette flow. *Phys. Rev. Lett.* **108**, 024501.

HUISMAN, S. G., SCHARNOWSKI, S., CIERPKA, C., KÄHLER, C., LOHSE, D. & SUN, C. 2013 Logarithmic boundary layers in strong Taylor–Couette turbulence. *Phys. Rev. Lett.* **110**, 264501.

HUISMAN, S. G., VAN DER VEEN, R. C. A., SUN, C. & LOHSE, D. 2014 Multiple states in highly turbulent Taylor–Couette flow. *Nat. Commun.* **5**, 3820.

JI, H., BURIN, M., SCHARTMAN, E. & GOODMAN, J. 2006 Hydrodynamic turbulence cannot transport angular momentum effectively in astrophysical disks. *Nature* **444**, 343–346.

KIEFER, J. 1953 Sequential minimax search for a maximum. *Proc. Am. Math. Soc.* **4**, 502–506.

KRAICHNAN, R. H. 1962 Turbulent thermal convection at arbritrary Prandtl number. *Phys. Fluids* **5**, 1374–1389.

LAKKARAJU, R., STEVENS, R. J. A. M., VERZICCO, R., GROSSMANN, S., PROSPERETTI, A., SUN, C. & LOHSE, D. 2012 Spatial distribution of heat flux and fluctuations in turbulent Rayleigh–Bénard convection. *Phys. Rev.* E **86**, 056315.

LATHROP, D. P., FINEBERG, J. & SWINNEY, H. S. 1992 Turbulent flow between concentric rotating cylinders at large Reynolds numbers. *Phys. Rev. Lett.* **68**, 1515–1518.

LEWIS, G. S. & SWINNEY, H. L. 1999 Velocity structure functions, scaling, and transitions in high-Reynolds-number Couette–Taylor flow. *Phys. Rev.* E **59**, 5457–5467.

LÓPEZ-CABALLERO, M. & BURGUETE, J. 2013 Inverse cascades sustained by the transfer rate of angular momentum in a 3D turbulent flow. *Phys. Rev. Lett.* **110**, 124501.

MALLOCK, A. 1896 Experiments on fluid viscosity. *Phil. Trans. R. Soc. Lond.* A **187**, 41–56.

MARUSIC, I., MONTY, J. P., HULTMARK, M. & SMITS, A. J. 2013 On the logarithmic region in wall turbulence. *J. Fluid Mech.* **716**, R3.

MERBOLD, S., BRAUCKMANN, H. J. & EGBERS, C. 2013 Torque measurements and numerical determination in differentially rotating wide gap Taylor–Couette flow. *Phys. Rev.* E **87**, 023014.

MERBOLD, S., FISCHER, S. & EGBERS, C. 2011 Torque scaling in Taylor–Couette flow – an experimental investigation. *J. Phys.: Conf. Ser.* **318** (8), 082017.

OSTILLA-MÓNICO, R., HUISMAN, S. G., JANNINK, T. J. G., VAN GILS, D. P. M., VERZICCO, R., GROSSMANN, S., SUN, C. & LOHSE, D. 2014*a* Optimal Taylor–Couette flow: radius ratio dependence. *J. Fluid Mech.* **747**, 1–29.

OSTILLA-MÓNICO, R., VAN DER POEL, E. P., VERZICCO, R., GROSSMANN, S. & LOHSE, D. 2014*b* Boundary layer dynamics at the transition between the classical and the ultimate regime of Taylor–Couette flow. *Phys. Fluids* **26** (1), 015114.

OSTILLA-MÓNICO, R., VAN DER POEL, E. P., VERZICCO, R., GROSSMANN, S. & LOHSE, D. 2014*c* Exploring the phase diagram of fully turbulent Taylor–Couette flow. *J. Fluid Mech.* **761**, 1–26.

OSTILLA-MÓNICO, R., VERZICCO, R., GROSSMANN, S. & LOHSE, D. 2016 The near-wall region of highly turbulent Taylor–Couette flow. *J. Fluid Mech.* **788**, 95–117.

PAOLETTI, M. S., VAN GILS, D. P. M., DUBRULLE, B., SUN, C., LOHSE, D. & LATHROP, D. P. 2012 Angular momentum transport and turbulence in laboratory models of Keplerian flows. *Astron. Astrophys.* **547**, A64.

VAN DER POEL, E. P., OSTILLA-MÓNICO, R., VERZICCO, R., GROSSMANN, S. & LOHSE, D. 2015 Logarithmic mean temperature profiles and their connection to plume emissions in turbulent Rayleigh–Bénard convection. *Phys. Rev. Lett.* **115**, 154501.

RAVELET, F., DELFOS, R. & WESTERWEEL, J. 2010 Influence of global rotation and Reynolds number on the large-scale features of a turbulent Taylor–Couette flow. *Phys. Fluids* **22** (5), 055103.

SHANG, X.-D., TONG, P. & XIA, K.-Q. 2008 Scaling of the local convective heat flux in turbulent Rayleigh–Bénard convection. *Phys. Rev. Lett.* **100**, 244503.

TAYLOR, G. I. 1923 Experiments on the motion of solid bodies in rotating fluids. *Proc. R. Soc. Lond.* A **104**, 213–218.

TOKGOZ, S., ELSINGA, G. E., DELFOS, R. & WESTERWEEL, J. 2011 Experimental investigation of torque scaling and coherent structures in turbulent Taylor–Couette flow. *J. Phys.: Conf. Ser.* **318** (8), 082018.

VAN DER VEEN, R. C. A., HUISMAN, S. G., DUNG, O.-Y., TANG, H. L., SUN, C. & LOHSE, D. 2016 Exploring the phase space of multiple states in highly turbulent Taylor–Couette flow. *Phys. Rev. Fluids* **1**, 024401.

WENDT, F. 1933 Turbulente Strömungen zwischen zwei rotierenden konaxialen Zylindern. *Ing.-Arch.* **4**, 577–595.